Precision Engineering 46 (2016) 73–80

Contents lists available at ScienceDirect

Precision Engineering

journal homepage: www.elsevier.com/locate/precision

A coupled dynamics, multiple degree of freedom process damping model, Part 2: Milling

Christopher T. Tyler, John R. Troutman, Tony L. Schmitz*

University of North Carolina at Charlotte, Charlotte, NC, United States

ARTICLE INFO

Article history:
Received 1 May 2015
Received in revised form 10 February 2016
Accepted 21 March 2016
Available online 11 May 2016

Keywords:
Machining
Chatter
Stability
Process damping
Simulation

ABSTRACT

Self-excited vibration, or chatter, is an important consideration in machining operations due to its direct influence on part quality, tool life, and machining cost. At low machining speeds, a phenomenon referred to as process damping enables stable cutting at higher depths of cut than predicted with traditional analytical models. This paper describes an analytical stability model for milling operations which includes a process damping force that depends on the surface normal velocity, depth of cut, cutting speed, and an empirical process damping coefficient. Model validation is completed using time domain simulation and milling experiments. The results indicate that the multiple degree of freedom model is able to predict the stability boundary using a single process damping coefficient.

1. Introduction

Process damping is a phenomenon that enables increased depths at cut at low cutting speeds in machining operations. When its effect is added to the analytical stability lobe diagram, a valuable predictive capability is afforded to process planners for a priori selection of machining parameters. It enables process planners to select stable {spindle speed, depth of cut} combinations for both:

- hard-to-machine materials, that are restricted to low cutting speeds due to prohibitive tool wear, and, therefore, cannot capitalize on the increased depths of cut observed in traditional stability lobe diagrams at higher spindle speeds; and
- high machinability materials that are able to take advantage of the increased depths of cut at the "best spindle speeds", which occur at rotating frequencies which are substantial integer fractions of the natural frequency that corresponds to the most flexible structural mode of vibration.

Nearly 50 years of experimental and theoretical investigations have yielded a phenomenological understanding of process damping. Pioneering work was completed by Wallace and Andrew [1], Sisson and Kegg [2], Peters et al. [3], and Tlusty [4]. These studies identified process damping as energy dissipation due to interference between the cutting tool relief, or clearance, face and the machined surface during the inherent relative vibration between the tool and workpiece. It was hypothesized that process damping increases at low cutting speeds because the number of undulations on the machined surface between revolutions (turning) or teeth (milling) increases, which also increases the slope of the wavy surface. This leads to increased interference and, consequently, increased energy dissipation.

Follow-on work has included a plowing force model based on interference between the tool's relief face and workpiece surface [5], application of the plowing force model to milling [6–9], a mechanistic description of the shearing and plowing force contributions to process damping [10], and a first-order Fourier transform representation of the tool-workpiece interference [11,12]. In [13,14], a numerical simulation of a nonlinear process damping stability model was presented, while [15] provided an experimental investigation of a nonlinear process damping model. Experimental identifications of a process damping model were presented in [16,17]. This study builds on the analyses presented in [18–20].

In this paper, an analytical stability analysis is presented that enables multiple degree of freedom (DOF) structural dynamics to be considered, while describing the process damping force in the surface normal direction as function of the depth of cut, the cutting speed, the tool velocity, and a single empirical coefficient. Because the process damping force is based on the surface normal velocity, which, in general, includes contributions from both orthogonal dynamics directions, a coupled dynamic system is obtained. The analytical solution for milling is presented in the following sections.

* Corresponding author. Tel.: +1 17046875086.
E-mail address: tony.schmitz@uncc.edu (T.L. Schmitz).

http://dx.doi.org/10.1016/j.precisioneng.2016.03.018
0141-6359/

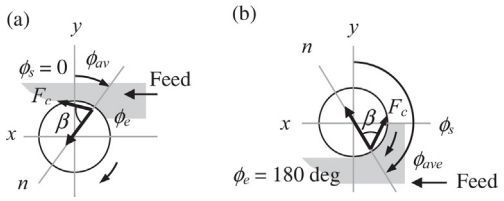

Fig. 1. Milling model for: (a) up milling (a 25% radial immersion cut is shown for illustrative purposes); (b) down milling (a 50% radial immersion cut is shown). The vector n defines the average surface normal direction and x is the feed direction.

Validation of the algorithm using time domain simulation and experiments is provided.

2. Stability algorithm

2.1. Single DOF in two directions

The milling model is depicted in Fig. 1, where x is the feed direction (the positive direction indicates the workpiece motion for a fixed tool position). The structural dynamics are measured in the x and y directions and may be described using lumped parameter mass, viscous damping, and stiffness values. The dynamics along the tool axis are not considered in this study. In this section, a single mode of vibration is assumed in the x and y directions.

As displayed in Fig. 1, the cutting force, F_c, is inclined relative to the surface normal, n, by the angle β. The surface normal is shown to be oriented at the average angle of a tooth in the cut, ϕ_{ave}, which is the mean of the cut starting, ϕ_s, and exit, ϕ_e, angles. These angles are defined by the milling operation (up/conventional or down/climb milling) and the radial depth of cut. The variable component of the cutting force is described by Eq. (1), where K_s is the specific cutting force coefficient that relates the cutting force to the chip area, b is the commanded axial depth of cut, N_0 is the vibration amplitude in the n direction from the previous revolution, and N is the current vibration amplitude. The difference between N_0 and N identifies the variable chip thickness due to the vibration from one revolution to the next and provides the basis for regenerative chatter. The mean component of the cutting force is excluded because it does not influence stability for the linear analysis presented here.

$$F_c = K_s b(N_0 - N) \tag{1}$$

The assumption for Eq. (1) is that there is no phase shift between the variable force and the chip thickness. This is indicated by the real values of b and K_s. However, it has been shown that a phase shift can occur at low cutting speeds. This phenomenon is captured by the inclusion of the process damping force, F_d, defined in Eq. (2) [17], where C is the process damping coefficient, V is the cutting speed, and $\dot{n}$ is the tool velocity in the n direction. The process damping force is oriented in the n direction and opposes the cutting force (as projected in the n direction). In other words, it is a viscous damping force; therefore, the process damping force is used to modify the structural damping and obtain an analytical stability solution.

$$F_d = -C\frac{b}{V}\dot{n} \tag{2}$$

To proceed with the solution, the cutting and process damping forces are projected into the x and y directions as shown in Eqs. (3) and (4), where $\phi_{ud} = 90 - \phi_{ave}$ for up milling and $\phi_{ud} = \phi_{ave} - 90$ for down milling.

$$F_x = F_c \cos\ (\beta + \phi_{ave} - 90) - C\frac{b}{V}\dot{n}\cos\ (\phi_{ud})$$

$$= F_{c_x} - C\frac{b}{V}\dot{n}\cos\ (\phi_{ud}) \tag{3}$$

$$F_y = F_c \cos\ (180 - \phi_{ave} - \beta) - C\frac{b}{V}\dot{n}\cos\ (180 - \phi_{ave})$$

$$= F_{c_y} - C\frac{b}{V}\dot{n}\cos\ (180 - \phi_{ave}) \tag{4}$$

The time domain equations of motion for the two directions are provided in Eqs. (5) and (6), where m_i, c_i, and k_i, $i = x, y$, are the mass, viscous damping coefficient, and stiffness for the single DOF structural dynamics. In these equations, one overdot indicates one time derivative (velocity) and two overdots indicate two time derivatives (acceleration).

$$m_x\ddot{x} + c_x\dot{x} + k_x x = F_{c_x} - C\frac{b}{V}\dot{n}\cos\ (\phi_{ud}) \tag{5}$$

$$m_y\ddot{y} + c_y\dot{y} + k_y y = F_{c_y} - C\frac{b}{V}\dot{n}\cos\ (180 - \phi_{ave}) \tag{6}$$

The n direction velocity can be written as a function of the velocities in the x and y directions as shown in Eq. (7). Substitution of Eq. (7) into Eqs. (5) and (6) yields Eqs. (8) and (9). Even though the structural dynamics are uncoupled (orthogonal), the equations of motion for the two directions are now coupled through the $\dot{x}$ and $\dot{y}$ velocity terms.

$$\dot{n} = \dot{x}\cos\ (\phi_{ud}) + \dot{y}\cos(180 - \phi_{ave}) \tag{7}$$

$$m_x\ddot{x} + c_x\dot{x} + k_x x = F_{c_x} - C\frac{b}{V}\cos\ (\phi_{ud})(\dot{x}\cos(\phi_{ud}) + \dot{y}\cos(180 - \phi_{ave})) \tag{8}$$

$$m_y\ddot{y} + c_y\dot{y} + k_y y = F_{c_y} - C\frac{b}{V}\cos\ (180 - \phi_{ave})(\dot{x}\cos(\phi_{ud}) + \dot{y}\cos(180 - \phi_{ave})) \tag{9}$$

By assuming solutions of the form $x(t) = Xe^{i\omega t}$ and $y(t) = Ye^{i\omega t}$ for harmonic motion, Eqs. (8) and (9) can be rewritten in the frequency domain (ω is frequency). The results are provided in Eqs. (10) and (11), where the X and Y terms have been grouped on the left hand side of both equations and the $e^{i\omega t}$ term has been dropped from both sides.

$$\left(-m_x\omega^2 + i\omega\left(c_x + C\frac{b}{V}(\cos(\phi_{ud}))^2\right) + k_x\right)X + i\omega\left(C\frac{b}{V}\cos\ (\phi_{ud})\cos(180 - \phi_{ave})\right)Y = F_{c_x} \tag{10}$$

$$\left(-m_y\omega^2 + i\omega\left(c_y + C\frac{b}{V}(\cos(180 - \phi_{ave}))^2\right) + k_y\right)Y + i\omega\left(C\frac{b}{V}\cos\ (\phi_{ud})\cos(180 - \phi_{ave})\right)X = F_{c_y} \tag{11}$$

These equations are arranged in matrix form as shown in Eq. (12), where:

- $a_{11} = \left(-m_x\omega^2 + i\omega\left(c_x + C\frac{b}{V}(\cos(\phi_{ud}))^2\right) + k_x\right)$
- $a_{12} = i\omega\left(C\frac{b}{V}\cos(\phi_{ud})\cos(180 - \phi_{ave})\right)$
- $a_{21} = a_{12}$
- $a_{22} = \left(-m_y\omega^2 + i\omega\left(c_y + C\frac{b}{V}(\cos(180 - \phi_{ave}))^2\right) + k_y\right)$.

$$\begin{bmatrix} a_{11} & a_{12} \\ a_{21} & a_{22} \end{bmatrix}\begin{bmatrix} X \\ Y \end{bmatrix} = \begin{bmatrix} F_{c_x} \\ F_{c_y} \end{bmatrix} \tag{12}$$

Using complex matrix inversion on a frequency-by-frequency basis, the direct and cross frequency response functions (FRFs) for the

coupled dynamic system are obtained as shown in Eq. (13). The direct FRFs are located in the on-diagonal positions and the cross FRFs are located in the off-diagonal positions; the cross FRFs are equal because the inverted matrix is symmetric.

$$\begin{bmatrix} X \\ Y \end{bmatrix} = \begin{bmatrix} a_{11} & a_{12} \\ a_{21} & a_{22} \end{bmatrix}^{-1} \begin{bmatrix} F_{c_x} \\ F_{c_y} \end{bmatrix} = \begin{bmatrix} \frac{X}{F_{c_x}} & \frac{X}{F_{c_y}} \\ \frac{Y}{F_{c_x}} & \frac{Y}{F_{c_y}} \end{bmatrix} \begin{bmatrix} F_{c_x} \\ F_{c_y} \end{bmatrix} \tag{13}$$

This work builds on the analytical stability solution presented by Tlusty [21]. As shown in Fig. 1, he assumed an average angle of the tooth in the cut and, therefore, an average cutting force direction. This produced an autonomous, or time invariant, system. He then made use of directional orientation factors, μ_x and μ_y, to first project this force into the x and y directions and, second, project these results into the surface normal, n (in the direction of ϕ_{ave}). The limiting axial depth of cut, b_{lim}, and spindle speed, Ω, are defined as a function of frequency using Eqs. (14) and (16), where $Re(G_{or})$ is the negative real part of the oriented FRF, N_t^* is the average number of teeth in the cut (see Eq. (16), where the angles are expressed in deg), f_c is the valid chatter frequencies (i.e., those frequencies where $Re(G_{or})$ is negative), N_t is the number of cutter teeth, $N = 0, 1, 2, \ldots$ is the integer number of waves between teeth (i.e., the lobe number), and $\varepsilon = 2\pi - 2\tan^{-1}(Re(G_{or})/Im(G_{or}))$ is the phase between the current vibration and the previous tooth. The spindle speed and limiting axial depth are plotted against one another to represent the stability boundary in traditional stability lobe diagrams.

$$b_{\text{lim}} = \frac{-1}{2K_s Re(G_{or}) N_t^*} \tag{14}$$

$$\frac{f_c}{\Omega N_t} = N + \frac{\varepsilon}{2\pi} \tag{15}$$

$$N_t^* = \frac{\phi_e - \phi_s}{360/N_t} \tag{16}$$

Tlusty's approach is extended here to develop an oriented FRF that incorporates both the direct and cross FRFs from Eq. (13). The oriented FRF is defined using Eq. (17), where μ_{ij}, $i, j = x, y$, are the directional orientation factors:

- $\mu_{xx} = \cos(\beta + \phi_{ave} - 90)\cos(\phi_{ud})$ projects F into x to cause x vibration through the direct FRF X/F_{c_x} and then projects this result into n
- $\mu_{xy} = \cos(180 - \beta + \phi_{ave})\cos(\phi_{ud})$ projects F into y to cause x vibration through the cross FRF X/F_{c_y} and then projects this result into n
- $\mu_{yx} = \cos(\beta + \phi_{ave} - 90)\cos(180 - \phi_{ave})$ projects F into x to cause y vibration through the cross FRF Y/F_{c_x} and then projects this result into n
- $\mu_{yy} = \cos(180 - \beta + \phi_{ave})\cos(180 - \phi_{ave})$ projects F into y to cause y vibration through the direct FRF Y/F_{c_y} and then projects this result into n.

$$G_{or} = \mu_{xx}\frac{X}{F_{c_x}} + \mu_{xy}\frac{X}{F_{c_y}} + \mu_{yx}\frac{Y}{F_{c_x}} + \mu_{yy}\frac{Y}{F_{c_y}} \tag{17}$$

The direct and cross FRFs included in Eq. (17) incorporate the process damping contribution by modifying the structural damping through the terms: $i\omega(c_x + C(b/V)(\cos(\phi_{ud}))^2)$, $i\omega(C(b/V)\cos(\phi_{ud})\cos(180 - \phi_{ave}))$, and $i\omega(c_y + C(b/V)(\cos(180 - \phi_{ave}))^2)$ as shown in Eq. (12). The process damping contribution depends on the b/V ratio in each case, where $V = (\pi d/60)\Omega$ (d is the tool diameter and Ω is expressed in rpm). Therefore, the b and Ω vectors must be known in order to modify the damping. This establishes a converging stability solution. The following steps are completed for each lobe number, N:

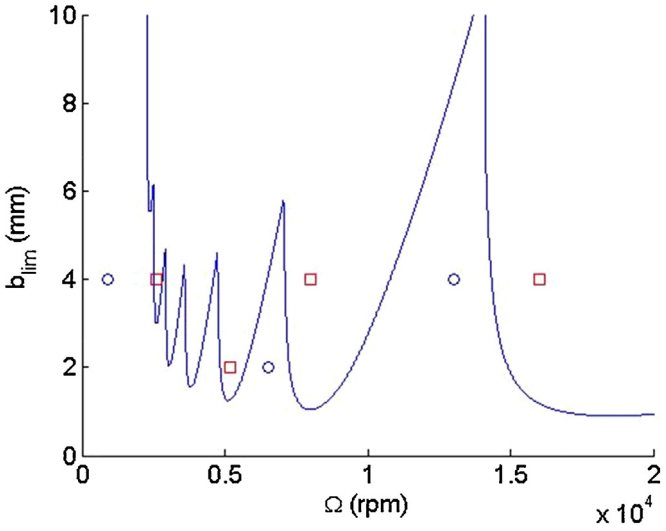

Fig. 2. Comparison of analytical stability limit and time domain simulation results for milling model with a single DOF in the x and y directions. Stable {spindle speed, chip width} combinations are identified by circles and unstable combinations are represented by squares.

1. the analytical stability boundary is calculated with no process damping to identify initial b and Ω vectors
2. these vectors are used to determine the process damping contribution
3. the stability analysis is repeated with the new damping terms to determine updated b and Ω vectors
4. the process is repeated until the stability boundary converges.

As shown in [18–20], the solution converges rapidly (20 iterations or less is typically sufficient).

To demonstrate the algorithm, consider the model in Fig. 1 with $\phi_s = 0$, $\phi_e = 90°$, $\beta = 70°$, $K_s = 2000\,\text{N/mm}^2$, $C = 200\,\text{N/mm}$, $N_t = 4$, and $d = 19\,\text{mm}$ for a 50% radial immersion up milling operation. The structural dynamics are symmetric in x and y with a stiffness of $9 \times 10^6\,\text{N/m}$, a natural frequency of 900 Hz, and a viscous damping ratio of 0.03 (3%). The corresponding stability limit with process damping effects is displayed in Fig. 2. To validate the predicted stability limit, Eqs. (5) and (6) were solved by Euler (numerical) integration in a time domain simulation [22]. Stable {spindle speed, chip width} combinations are identified by circles and unstable combinations are represented by squares in Fig. 2. Good agreement is observed.

2.2. Two DOF in two directions

The coupled dynamics solution is now extended to two DOF in the x and y directions. From an FRF measurement in each direction, the modal parameters can be extracted (by peak picking, for example) which represent uncoupled single DOF systems in the modal coordinates q_1 and q_2 for the x direction and p_1 and p_2 for the y direction [22]. This modal representation requires that proportional damping holds, but this is a reasonably approximation for the lightly damped tool point dynamics typically observed in practice.

Eq. (5), which provides the equation of motion for the x direction with a single DOF, is rewritten in Eq. (18) to describe motion in the first modal DOF, q_1. The n direction velocity is again $\dot{n} = \dot{x}\cos(\phi_{ud}) + \dot{y}\cos(180 - \phi_{ave})$, but $\dot{x}$ is now the sum of the modal

velocities, $\dot{x} = \dot{q}_1 + \dot{q}_2$ and $\dot{y} = \dot{p}_1 + \dot{p}_2$. Substitution yields Eq. (19). Eqs. (20) and (21) give the results for q_2 motion (the second modal DOF) in the x direction.

$$m_{q_1}\ddot{q}_1 + c_{q_1}\dot{q}_1 + k_{q_1}q_1 = F_{c_x} - C\frac{b}{V}\dot{n}\cos\ (\phi_{ud}) \tag{18}$$

$$m_{q_1}\ddot{q}_1 + c_{q_1}\dot{q}_1 + k_{q_1}q_1 = F_{c_x} - C\frac{b}{V}\cos\ (\phi_{ud})(\cos(\phi_{ud})(\dot{q}_1 + \dot{q}_2) + \cos(180 - \phi_{ave})(\dot{p}_1 + \dot{p}_2)) \tag{19}$$

$$m_{q_2}\ddot{q}_2 + c_{q_2}\dot{q}_2 + k_{q_2}q_2 = F_{c_x} - C\frac{b}{V}\dot{n}\cos\ (\phi_{ud}) \tag{20}$$

$$m_{q_2}\ddot{q}_2 + c_{q_2}\dot{q}_2 + k_{q_2}q_2 = F_{c_x} - C\frac{b}{V}\cos\ (\phi_{ud})(\cos(\phi_{ud})(\dot{q}_1 + \dot{q}_2) + \cos(180 - \phi_{ave})(\dot{p}_1 + \dot{p}_2)) \tag{21}$$

Eqs. (19) and (21) are converted to the frequency domain by again assuming harmonic motion so that $q_j(t) = Q_j e^{i\omega t}$ and $p_j(t) = P_j e^{i\omega t}$, $j = 1, 2$. Eq. (22) represents motion in Q_1 and Eq. (23) describes motion in Q_2. Even though the modal degrees of freedom are uncoupled by definition, the two equations of motion for the x direction now include both Q_1 and Q_2 due to process damping. Similar to the single DOF model in the previous section, the equations also include contributions from the y direction dynamics (P_1 and P_2). As with turning, the equations of motion are coupled in both modal coordinates and the two orthogonal directions [23].

$$\left(-m_{q_1}\omega^2 + i\omega\left(c_{q_1} + C\frac{b}{V}(\cos(\phi_{ud}))^2\right) + k_{q_1}\right)Q_1 + i\omega\left(C\frac{b}{V}(\cos(\phi_{ud}))^2\right)Q_2 + i\omega\left(C\frac{b}{V}(\cos(\phi_{ud}))\cos(180 - \phi_{ave})\right)(P_1 + P_2) = F_{c_x} \tag{22}$$

$$\left(-m_{q_2}\omega^2 + i\omega\left(c_{q_2} + C\frac{b}{V}(\cos(\phi_{ud}))^2\right) + k_{q_2}\right)Q_2 + i\omega\left(C\frac{b}{V}(\cos(\phi_{ud}))^2\right)Q_1 + i\omega\left(C\frac{b}{V}\cos\ (\phi_{ud})\cos(180 - \phi_{ave})\right)(P_1 + P_2) = F_{c_x} \tag{23}$$

Following the same approach, the frequency domain equations for the y direction are presented in Eqs. (24) and (25), where Eq. (24) describes motion in P_1 and Eq. (25) describes motion in P_2.

$$\left(-m_{p_1}\omega^2 + i\omega\left(c_{p_1} + C\frac{b}{V}(\cos(180 - \phi_{ave}))^2\right) + k_{p_1}\right)P_1 + i\omega\left(C\frac{b}{V}(\cos(180 - \phi_{ave}))^2\right)P_2 + i\omega\left(C\frac{b}{V}\cos\ (\phi_{ud})\cos(180 - \phi_{ave})\right)(Q_1 + Q_2) = F_{c_y} \tag{24}$$

$$\left(-m_{p_2}\omega^2 + i\omega\left(c_{p_2} + C\frac{b}{V}(\cos(180 - \phi_{ave}))^2\right) + k_{p_2}\right)P_2 + i\omega\left(C\frac{b}{V}(\cos(180 - \phi_{ave}))^2\right)P_1 + i\omega\left(C\frac{b}{V}\cos\ (180 - \phi_{ave})\cos(\phi_{ud})\right)(Q_1 + Q_2) = F_{c_2} \tag{25}$$

Eqs. (22)–(25) are arranged in matrix form as shown in Eq. (26), where:

- $a_{11} = \left(-m_{q_1}\omega^2 + i\omega\left(c_{q_1} + C\frac{b}{V}(\cos(\phi_{ud}))^2\right) + k_{q_1}\right)$
- $a_{12} = i\omega\left(C\frac{b}{V}(\cos(\phi_{ud}))^2\right)$
- $a_{13} = i\omega\left(C\frac{b}{V}\cos(\phi_{ud})\cos(180 - \phi_{ave})\right)$
- $a_{14} = i\omega\left(C\frac{b}{V}\cos(\phi_{ud})\cos(180 - \phi_{ave})\right)$
- $a_{21} = a_{12}$
- $a_{22} = \left(-m_{q_2}\omega^2 + i\omega\left(c_{q_2} + C\frac{b}{V}(\cos(\phi_{ud}))^2\right) + k_{q_2}\right)$
- $a_{23} = i\omega\left(C\frac{b}{V}\cos(\phi_{ud})\cos(180 - \phi_{ave})\right)$
- $a_{24} = i\omega\left(C\frac{b}{V}\cos(\phi_{ud})\cos(180 - \phi_{ave})\right)$
- $a_{31} = a_{13}$
- $a_{32} = a_{23}$
- $a_{33} = \left(-m_{p_1}\omega^2 + i\omega\left(c_{p_1} + C\frac{b}{V}(\cos(180 - \phi_{ave}))^2\right) + k_{p_1}\right)$
- $a_{34} = i\omega\left(C\frac{b}{V}\cos(\phi_{ud})\cos(180 - \phi_{ave})\right)$
- $a_{41} = a_{14}$
- $a_{42} = a_{24}$
- $a_{43} = a_{34}$
- $a_{44} = \left(-m_{p_2}\omega^2 + i\omega\left(c_{p_2} + C\frac{b}{V}(\cos(180 - \phi_{ave}))^2\right) + k_{p_2}\right)$.

$$\begin{bmatrix} a_{11} & a_{12} & a_{13} & a_{14} \\ a_{21} & a_{22} & a_{23} & a_{24} \\ a_{31} & a_{32} & a_{33} & a_{34} \\ a_{41} & a_{42} & a_{43} & a_{44} \end{bmatrix} \begin{bmatrix} Q_1 \\ Q_2 \\ P_1 \\ P_2 \end{bmatrix} = \begin{bmatrix} F_{c_x} \\ F_{c_x} \\ F_{c_y} \\ F_{c_y} \end{bmatrix} \tag{26}$$

Using complex matrix inversion on a frequency-by-frequency basis, the direct and cross frequency response functions (FRFs) for the coupled dynamic system are obtained as shown in Eq. (27).

$$\begin{bmatrix} Q_1 \\ Q_2 \\ P_1 \\ P_2 \end{bmatrix} = \begin{bmatrix} a_{11} & a_{12} & a_{13} & a_{14} \\ a_{21} & a_{22} & a_{23} & a_{24} \\ a_{31} & a_{32} & a_{33} & a_{34} \\ a_{41} & a_{43} & a_{43} & a_{44} \end{bmatrix}^{-1} \begin{bmatrix} F_{c_x} \\ F_{c_x} \\ F_{c_y} \\ F_{c_y} \end{bmatrix} = \begin{bmatrix} \frac{Q_{1,1}}{F_{c_x}} & \frac{Q_{1,2}}{F_{c_x}} & \frac{Q_{1,3}}{F_{c_y}} & \frac{Q_{1,4}}{F_{c_y}} \\ \frac{Q_{2,1}}{F_{c_x}} & \frac{Q_{2,2}}{F_{c_x}} & \frac{Q_{2,3}}{F_{c_y}} & \frac{Q_{2,4}}{F_{c_y}} \\ \frac{P_{1,1}}{F_{c_x}} & \frac{P_{1,2}}{F_{c_x}} & \frac{P_{1,3}}{F_{c_y}} & \frac{P_{1,4}}{F_{c_y}} \\ \frac{P_{2,1}}{F_{c_x}} & \frac{Q_{2,2}}{F_{c_x}} & \frac{P_{2,3}}{F_{c_y}} & \frac{P_{2,4}}{F_{c_y}} \end{bmatrix} \begin{bmatrix} F_{c_x} \\ F_{c_x} \\ F_{c_y} \\ F_{c_y} \end{bmatrix} \tag{27}$$

The direct FRFs in the x and y directions are defined by Eqs. (28) and (29), respectively; the cross FRFs are provided in Eqs. (30) and (31). The oriented FRF is again calculated using Eq. (17); the directional orientation factors are the same.

$$\frac{X}{F_{c_x}} = \frac{Q_{1,1}}{F_{c_x}} + \frac{Q_{1,2}}{F_{c_x}} + \frac{Q_{2,1}}{F_{c_x}} + \frac{Q_{2,2}}{F_{c_x}} \tag{28}$$

$$\frac{Y}{F_{c_y}} = \frac{P_{1,3}}{F_{c_y}} + \frac{P_{1,4}}{F_{c_y}} + \frac{P_{2,3}}{F_{c_y}} + \frac{P_{2,4}}{F_{c_y}} \tag{29}$$

$$\frac{y}{F_{c_x}} = \frac{P_{1,1}}{F_{c_x}} + \frac{P_{1,2}}{F_{c_x}} + \frac{P_{2,1}}{F_{c_x}} + \frac{P_{2,2}}{F_{c_x}} \tag{30}$$

$$\frac{X}{F_{c_y}} = \frac{Q_{1,3}}{F_{c_y}} + \frac{Q_{1,4}}{F_{c_y}} + \frac{Q_{2,3}}{F_{c_y}} + \frac{Q_{2,4}}{F_{c_y}} \tag{31}$$

The model may be extended to additional DOFs in each direction. For three DOFs in each direction, for example, Eq. (26) becomes a 6×6 symmetric matrix. The direct and cross FRFs are then a sum of six, rather than four, terms from the inverted matrix.

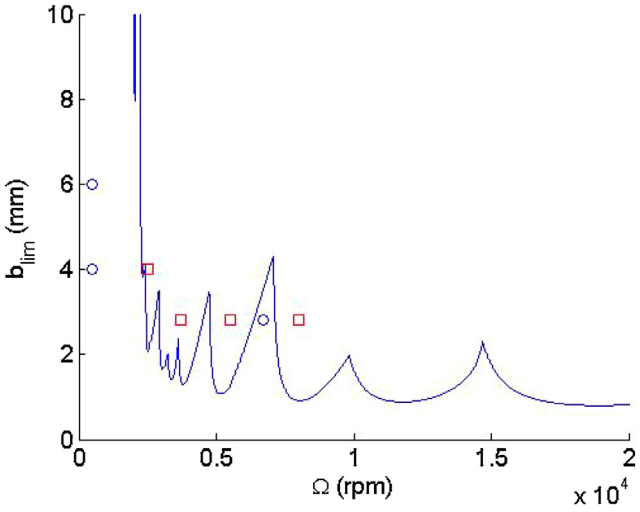

Fig. 3. Comparison of analytical stability limit and time domain simulation results for milling model with two DOF in the *x* and *y* directions.

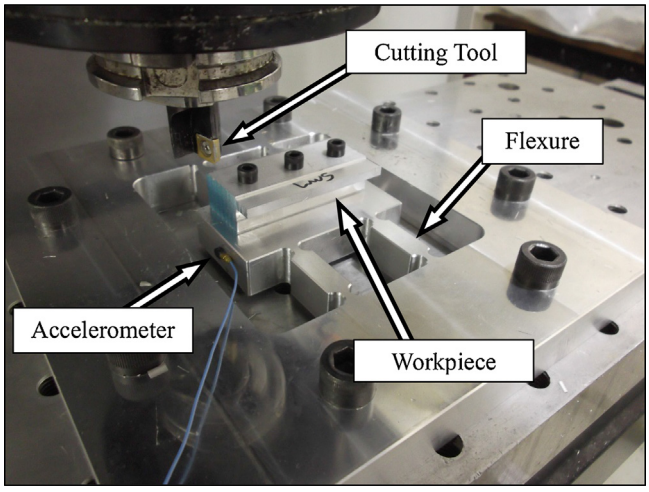

Fig. 4. Experimental setup for single DOF milling stability tests. An accelerometer was used to monitor the flexure vibration during machining.

To demonstrate the algorithm, consider the model in Fig. 1 with $\phi_s = 0, \phi_e = 90^\circ, \beta = 70^\circ, K_s = 2000\,\text{N/mm}^2, C = 200\,\text{N/mm}, N_t = 4$, and $d = 19\,\text{mm}$ for a 50% radial immersion up milling operation. The structural dynamics are symmetric with a modal stiffness of $7 \times 10^6\,\text{N/m}$, a natural frequency of 700 Hz, and a viscous modal damping ratio of 0.03 (3%) for the first mode and a modal stiffness of $9 \times 10^6\,\text{N/m}$, a natural frequency of 900 Hz, and a viscous modal damping ratio of 0.03 (3%) for the second mode. The corresponding stability limit with process damping effects is displayed in Fig. 3. To validate the predicted stability limit, the modal equations of motion were solved by Euler (numerical) integration in a time domain simulation [22]. Stable {spindle speed, chip width} combinations are identified by circles and unstable combinations are represented by squares in Fig. 3. Good agreement is observed.

3. Experimental setup

To validate the multiple degree of freedom process damping model for milling, low-speed cutting tests were performed and a process damping coefficient was calculated. Experiments were performed on a Haas TM-1 CNC milling machine. Two custom-designed notch hinge flexures, pictured in Figs. 4 and 5, were designed. The flexure in Fig. 4 provided a single DOF in the feed direction, while Fig. 5 yielded two DOF. To negate the effects of tool dynamics, tool corner radius effects, and interaction between the tool end and the machined floor, a fin geometry was selected for the workpiece. Using this configuration, analogous to the tube turning experiments presented in [23], the tool is much stiffer than the workpiece/flexure system; because the flexure is intentionally more compliant than the tool along the feed direction, the stability analysis was performed using the modal parameters of the workpiece/flexure system. Table 1 and Figs. 6 and 7 provide the modal parameters and the frequency response function for the workpiece/flexure systems along the *x* (feed) and *y* directions. These

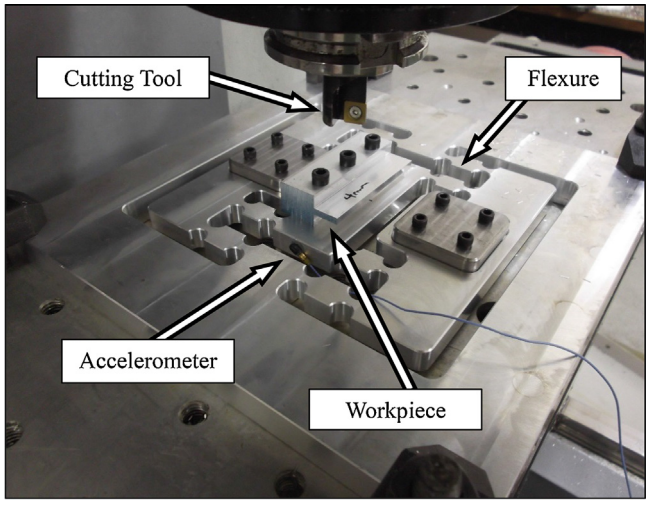

Fig. 5. Experimental setup for multiple DOF milling stability tests. An accelerometer was used to monitor the flexure vibration during machining.

Table 1
Modal parameters for workpiece/flexure setups.

Direction	Viscous damping ratio (%)	Modal stiffness ($\times 10^7$ N/m)	Natural frequency (Hz)
	Single DOF milling setup		
y	1.56	3.85	1532
x	0.47	0.890	815
	Multiple DOF milling setup		
y	1.82	4.208	1678
x	0.37	0.814	515
	0.14	2.871	1408

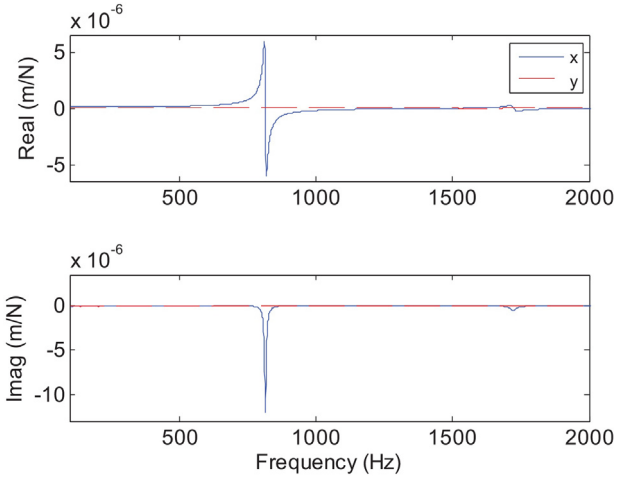

Fig. 6. Frequency response function for the single DOF workpiece/flexure system in the *x* (feed) and *y* directions.

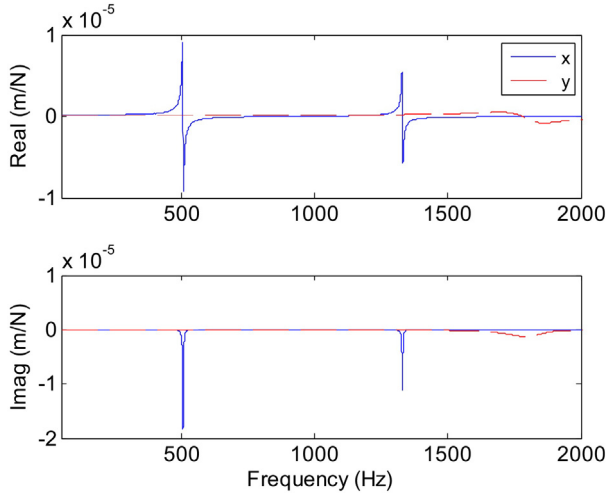

Fig. 7. Frequency response function for the multiple DOF workpiece/flexure system in the *x* (feed) and *y* directions.

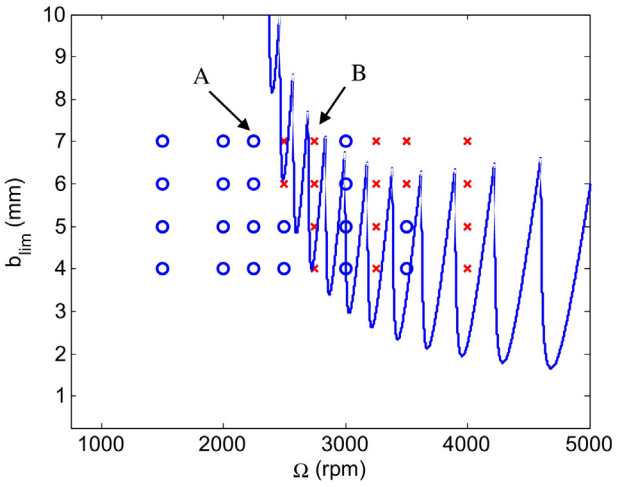

Fig. 8. Grid of stable (o) and unstable (x) test points with the final stability boundary corresponding to $C = 1.70 \times 10^5$ N/m for the single DOF setup.

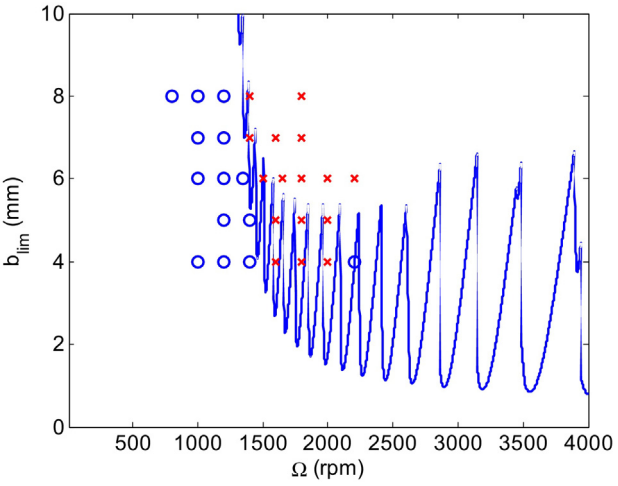

Fig. 9. Stability boundary for the multiple DOF system ($C = 1.80 \times 10^5$ N/m).

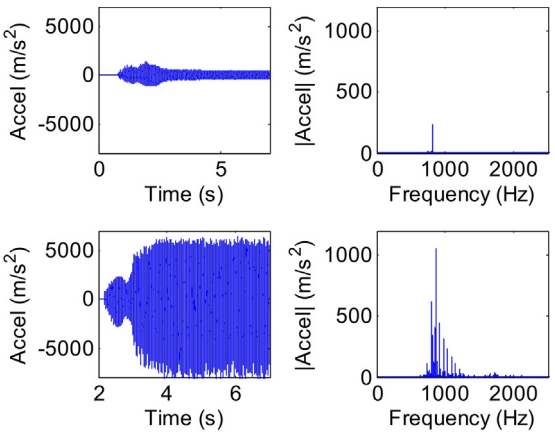

Fig. 10. Accelerometer time domain signals for stable (top left) and unstable (bottom left) cutting parameters and the corresponding frequency domain stable (top right) and unstable (bottom right) signals for the single DOF system.

were determined using impact testing, where an instrumented hammer is used to excite the structure and the response is measured using a linear transducer (a low mass accelerometer in this case).

For all cutting tests, the workpiece material was 6061-T6 aluminum. A 19 mm (0.75 in) diameter single-flute inserted endmill was used with a TiN coated insert (Kennametal SPEB322); the insert had a 0° rake angle, an 11° relief angle, and no chip breaker.[1] The fin thickness was varied, corresponding to axial depths of cut, *b*, from 4 mm to 8 mm. Radial engagement was held constant for all tests at 4.75 mm (25% of the tool diameter), while a constant feedrate of 0.05 mm per tooth was maintained.

The specific cutting force for the workpiece/tool combination was also determined. Using the same tool, a test coupon of identical material, cut from the same stock as the finned specimens, was mounted to a cutting force dynamometer (Kistler 9257B). At 1000 rpm and feedrates from 0.010 mm/tooth to 0.076 mm/tooth, the specific cutting force was 1368 N/mm^2 with a force angle of 50.7°.

4. Experimental results

Experiments were performed at selected low-speed test points. At each point, the stability of the cut was determined by monitoring the flexure vibration using an accelerometer (PCB 353B14). An experimental process damping coefficient, *C*, was estimated from a residual sum of squares (RSS) minimization of points which best represent the stability boundary. A process damping coefficient value of $C = 1.70 \times 10^5$ N/m was obtained for the single DOF setup and a value of $C = 1.80 \times 10^5$ N/m for the multiple DOF setup. The stable (o) and unstable (x) test points and stability boundary are presented in Figs. 8 and 9, respectively.

Points A and B in Fig. 8 were selected to illustrate stable and unstable cutting characteristics. Fig. 10 (top) shows the time and frequency domain accelerometer signal at point A, a stable cut at 2000 rpm, $b = 7$ mm. The time domain acceleration signal settles to a small vibration amplitude after entering the cut. The frequency content of the signal includes a small peak close to the system's natural frequency of 815 Hz. Fig. 10 (bottom) displays the time and frequency domain measurement signals at point B, an unstable cut at 2750 rpm, $b = 7$ mm. The time domain acceleration signal for this unstable cut grows rapidly after entering the cut. The frequency content of the unstable test cut includes a larger magnitude chatter frequency, again, near the system's natural frequency. Similar

[1] The edge radius was not measured, but neither was the commercial insert initial edge geometry modified.

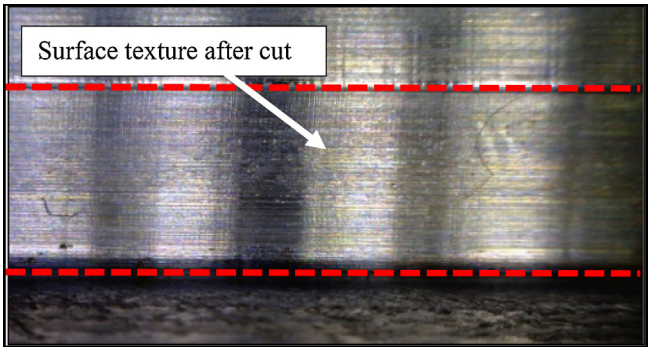

Fig. 11. Workpiece surface finish after a stable cut.

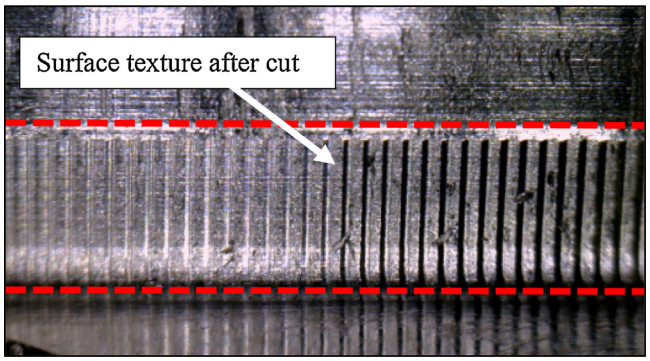

Fig. 12. Workpiece surface finish after an unstable cut.

analyses were performed using the signals from the multiple DOF tests.

In addition to vibration measurements, the surface of the workpiece was analyzed visually after each test cut. Qualitatively, the surface texture of a stable cut exhibited very few surface flaws; see Fig. 11. Inspection of the workpiece surface for an unstable cut revealed irregular vibratory flaws due to the self-excited cutter vibration; see Fig. 12.

Examining the results from the single and multiple DOF tests, it is observed that there is relatively low variability in the process damping coefficient values between the two milling setups. The process damping coefficient changed by less than 6% between the single DOF and multiple DOF experiments. This suggests that the same process damping coefficient can be used for a range of dynamic systems.

Table 2
Process damping coefficients for the 11° relief angle tool geometry.

Material	Process damping coefficient, C (N/m)	
	Low insert wear (FWW < 0.100 μm)	Moderate insert wear (0.150 μm < FWW < 0.250 μm)
1018 steel	1.65×10^5	2.00×10^5
Ti 6Al–4V	1.70×10^5	1.80×10^5
304 SS	5.20×10^5	5.80×10^5
Inconel 718	1.20×10^5	1.05×10^5

Table 3
Process damping coefficients for the 15° relief angle tool geometry.

Material	Process damping coefficient, C (N/m)	
	Low insert wear (FWW < 0.100 μm)	Moderate insert wear (0.150 μm < FWW < 0.250 μm)
1018 steel	1.25×10^5	1.50×10^5
Ti 6Al–4V	1.20×10^5	1.40×10^5
304 SS	4.10×10^5	4.50×10^5
Inconel 718	1.00×10^5	1.30×10^5

5. Generating a process coefficient database

With a technique in place to experimentally quantify the low-speed stability behavior due to process damping and the ability to portray the low-speed stability boundary using a single coefficient, a database of the process modeling coefficients was established for several representative hard-to-machine materials. AISI 1018 steel, Ti 6Al–4V, AISI 304 stainless steel, and Inconel 718 were selected to populate the database, based on their growing use in the medical, aerospace, and energy manufacturing sectors.

The database includes the process damping model coefficient and specific cutting force values. The process damping effect has been shown to be influenced by tool geometry, e.g., relief angle and tool wear [9,11]. Therefore, the coefficients are provided for two relief angles (11° and 15°) at both low and moderate wear states of the cutting edge (identified using the flank wear width, FWW). All process damping coefficients were collected using a single DOF flexure setup. The specific cutting force values were measured using a linear regression technique [22]. The cutting conditions were 50% radial immersion up milling for the mild steel and 25% radial depth of cut down milling for the others. This increased the allowable depths of cut for the harder materials and eliminated chip welding to the machined surface. The database of process modeling coefficients is presented in Tables 2–5.

Table 4
Specific cutting force values for the 11° relief angle tool geometry.

Material	Low insert wear (FWW < 0.100 μm)		Moderate insert wear (0.150 μm < FWW < 0.250 μm)	
	K_s (N/mm^2)	β (°)	K_s (N/mm^2)	β (°)
1018 steel	2531.0	62.0	2550.2	62.0
Ti 6Al–4V	2107.0	66.0	2131.2	60.1
304 SS	3318.0	62.5	3517.0	61.0
Inconel 718	3515.0	61.1	3617.0	60.6

Table 5
Specific cutting force values for the 15° relief angle tool geometry.

Material	Low insert wear (FWW < 0.100 μm)		Moderate insert wear (0.150 μm < FWW < 0.250 μm)	
	K_s (N/mm^2)	β (°)	K_s (N/mm^2)	β (°)
1018 steel	2359.1	63.5	2441.0	63.5
Ti 6Al–4V	2076.3	66.7	2247.2	56.3
304 SS	3427.2	63.1	3503.2	61.5
Inconel 718	3582.0	62.0	3653.0	63.0

From Tables 2 and 3, it is observed that the process damping force coefficient increases with progressive wear and decreases with a larger relief angle; a larger C value indicates increased process damping. Both trends support the general description of process damping as interference between the relief face and machined surface. Increased flank wear reduces the apparent relief angle local to the cutting edge. A smaller relief angle, whether by design or wear, encourages the interference phenomenon.

For the specific cutting force coefficient, K_s, no clear trend is apparent for a change in the tool geometry. The largest difference for relief angle variation is 6.8% (1018 steel). The largest difference due to the wear level is −8.2% (15° relief angle tool, 6Al–4V titanium).

6. Conclusions

An analytical stability model for multiple degree of freedom milling was presented. This dynamic model includes contributions from the frequency response functions for the vibratory system, as well as a process damping force which is a function of the velocity in the surface normal direction, depth of cut, cutting speed, and an empirically-determined process damping coefficient, C. The model was evaluated using time-domain simulation and experiments. Stability tests were performed using custom single DOF and multiple DOF parallelogram notch hinge flexures; finned 6061-T6 aluminum workpieces were mounted to the flexures. The flexure/workpiece system vibration during cutting was used to determine the process stability at selected spindle speed and axial depth of cut combinations. Process damping coefficients of $C = 1.7 \times 10^5$ N/m and 1.8×10^5 N/m were calculated using RSS minimization to best fit the stability boundary for single and multiple DOF setups, respectively. The low variability between the different dynamic systems suggests that the same process damping coefficient can be used for a range of flexible cutting systems.

The technique used to experimentally identify the process damping coefficients was then used to populate a process coefficient database. This database includes specific cutting force and process damping values for AISI 1018 steel, Ti 6Al–4V, AISI 304 stainless steel, and Inconel 718.

Hard-to-machine materials often dictate low cutting speeds due to tool wear restrictions. When sufficient machine power is available, operation in the low-speed process damping regime can significantly boost productivity. Knowledge of process damping coefficients for a given material enables pre-process selection of optimum machining parameters.

Acknowledgements

The authors gratefully acknowledge partial financial support from the University of North Carolina at Charlotte Center for Precision Metrology Affiliates Program.

References

Wallace, P.W., Andrew, C., 1965. Machining forces: some effects of tool vibration. J Mech Eng Sci 7, 152–162.
Sisson, T.R., Kegg, R.L., 1969. An explanation of low-speed chatter effects. J Eng Ind 91, 951–958.
Peters, J., Vanherck, P., Van Brussel, H., 1971. The measurement of the dynamic cutting coefficient. Ann CIRP 21 (2), 129–136.
Tlusty, J., 1978. Analysis of the state of research in cutting dynamics. Ann CIRP 27 (2), 583–589.
Wu, D.W., 1989. A new approach of formulating the transfer function for dynamic cutting processes. J Eng Ind 111, 37–47.
Elbestawi, M.A., Ismail, F., Du, R., Ullagaddi, B.C., 1994. Modelling machining dynamics damping in the tool-workpiece interface. J Eng Ind 116, 435–439.
Lee, B.Y., Trang, Y.S., Ma, S.C., 1995. Modeling of the process damping force in chatter vibration. Int J Mach Tools Manuf 35, 951–962.
Abraria, F., Elbestawi, M.A., Spencea, A.D., 1998. On the dynamics of ball end milling: modeling of cutting forces and stability analysis. Int J Mach Tools Manuf 38, 215–237.
Ahmadi, K., Ismail, F., 2010. Machining chatter in flank milling. Int J Mach Tools Manuf 50, 75–85.
Huang, C.Y., Wang, J.J., 2007. Mechanistic modeling of process damping in peripheral milling. J Manuf Sci Eng 129, 12–20.
Chiou, Y.S., Chung, E.S., Liang, S.Y., 1995. Analysis of tool wear effect on chatter stability in turning. Int J Mech Sci 37, 391–404.
Chiou, R.Y., Liang, S.Y., 1998. Chatter stability of a slender cutting tool in turning with tool wear effect. Int J Mach Tools Manuf 38, 315–327.
Chandiramani, N.K., Pothala, T., 2006. Dynamics of 2-dof regenerative chatter during turning. J Sound Vib 290, 448–464.
Jemielniak, K., Widota, A., 1989. Numerical simulation of non-linear chatter vibration in turning. Int J Mach Tools Manuf 29, 239–247.
Ahmadi, K., Ismail, F., 2010. Experimental investigation of process damping nonlinearity in machining chatter. Int J Mach Tools Manuf 50, 1006–1014.
Budak, E., Tunc, L.T., 2009. A new method for identification and modeling of process damping in machining. J Manuf Sci Eng 131, 051019/1–051019/51019.
Altintas, Y., Eynian, M., Onozuka, H., 2008. Identification of dynamic cutting force coefficients and chatter stability with process damping. Ann CIRP 57 (1), 371–374.
Tyler, C., Schmitz, T., 2012. Process damping analytical stability analysis and validation. Trans NAMRI/SME 40.
Tyler, C., Karandikar, J., T. Schmitz, T., 2013. Process damping coefficient identification using Bayesian inference. Trans NAMRI/SME 41.
Tyler, C., Schmitz, T., 2013. Analytical process damping stability prediction. J Manuf Process 15, 69–76.
Tlusty, J., Zaton, W., Ismail, F., 1983. Stability lobes in milling. Ann CIRP 32 (1), 309–313.
Schmitz, T., Smith, S., 2009. Machining dynamics: frequency response to improved productivity. Springer, New York, NY.
Tyler, C., Troutman, J., Schmitz, T., 2016. A coupled dynamics, multiple degree of freedom process damping model, Part 1: Turning. Precis Eng 46, 65–72.